PNAS

Supplementary Information for

Intrinsically disordered interaction network in an RNA chaperone revealed by native mass spectrometry.

Samantha H. Sarni[1†] (1), Jorjethe Roca[2] (1), Chen Du[1], Mengxuan Jia[1‡], Hantian Li[2], Ana Damjanovic[2], Ewelina M. Małecka[2], Vicki H. Wysocki[1*], Sarah A. Woodson[2*]

Vicki H. Wysocki or Sarah A. Woodson
Email: wysocki.11@osu.edu or swoodson@jhu.edu

This PDF file includes:

Other supplementary materials for this manuscript include the following:

Supplementary Information Text

SI Materials and Methods

Mass spectrometry. Nano-electrospray ionization (nESI) emitters were prepared in-house using a Sutter P-97 micropipette puller. 3-6 µL samples were loaded into the nESI emitters using a Hamilton 10 µL syringe or ultra-micro gel loading pipette tips. All spectra in this work were acquired on a Waters Synapt G2 HDMS instrument (Waters Corporation, Wilmslow, U.K.) modified with a surface-induced dissociation (SID) device, as described previously (1). Briefly, a custom SID device was inserted between a shortened trap stacked ring ion guide and an ion mobility cell. Voltages were supplied to the SID cell via external DC power supplies (Ardara Technologies, Ardara, PA) and controlled through the accompanying Tempus Tune software (Ardara Technologies, Ardara, PA). SID lenses can be tuned either to transmit ions for MS or to direct the ions onto the surface for collision. Typical settings used here for transmission mode and SID can be found in Tables S4-S5. Energy resolved mass spectra (ERMS) were produced by acquiring data from tandem MS experiments with SID voltage potentials ranging from 15 and 140 V. The precursor charge state for SID experiments was chosen as the lowest available charge state (which retains native-like state more reliably) that has a stable enough signal intensity for 21 different SID spectra. Each experiment was repeated in technical triplicate.

Analysis of mass spectrometry data. The expected molecular masses of monomer Hfq and RNAs were calculated using the UniDec Protein/RNA mass calculator (2). Selection rules, arrival time, and *m/z* were made for each SID product using Waters Corporation Driftscope 2.9 software. The intensity of each subcomplex respective charge state was then extracted from each series of SID spectra using TWIMExtract v1.3 (3). The intensities of all charge states of each SID product were summed and averaged for three replicates and plotted with standard error. Due to the sparse nature of the mass spectra, the ERMS data underwent a linear interpolation processing step to create the continuous data needed for comparing differences in dissociation energies. The mean of the error of data points in individual ERMS was assigned as the error of the interpolated data. Collision energies were calculated as $E(eV) = zV_{SID}$; where z is the charge state of the precursor ions and V_{SID} is the SID voltage defined as the potential difference between the trap exit and the surface. To eliminate the mass difference between HfqΔCTD and Hfq, the collision energies for Hfq were corrected by a factor (4), to yield:

$$E_{Hfq}^{mass-corrected} = \frac{m_{Hfq\Delta CTD}}{m_{Hfq}} E_{Hfq} \quad \text{(S1)}$$

in which $m_{Hfq\Delta CTD}$ and m_{Hfq} are the masses of HfqΔCTD and Hfq, respectively, and E_{Hfq} is the collision energy of Hfq. Collision energies for protein-RNA complexes were also corrected to account for the mass of the bound RNA:

$$E_{Hfq\Delta CTD+RNA}^{mass-corrected} = \frac{m_{Hfq\Delta CTD}}{m_{Hfq\Delta CTD+RNA}} E_{Hfq\Delta CTD+RNA} \quad \text{(S2)}$$

$$E_{Hfq+RNA}^{mass-corrected} = \frac{m_{Hfq\Delta CTD}}{m_{Hfq+RNA}} E_{Hfq+RNA} \quad \text{(S3)}$$

in which $m_{Hfq\Delta CTD+RNA}$ and $m_{Hfq+RNA}$ are the masses of HfqΔCTD and Hfq bound to RNA, respectively, and $E_{Hfq\Delta CTD+RNA}$ and $E_{Hfq+RNA}$ are the collision energies of the complexes of HfqΔCTD and Hfq bound to RNA.

Surface-induced unfolding (SIU) plots were generated by extracting and normalizing the intensity of the respective precursor ion using TWIMExtract and ORIGAMI 1.2.1.6 (5).

Errors in collision energy difference (ΔCE) plots (Figs. 4*C, E,* and *G*) were propagated as $\sigma(\Delta CE) = \sqrt{\sigma^2(CE_{Protein\bullet RNA}) + \sigma^2(CE_{Protein})}$; where σ^2 is the spread of the ERMS interpolated

data on the collision energy axis (Figs. 4*B* and *4D*). Errors for Fig. 4*G*, were calculated similarly but for Hfq•RNA - HfqΔCTD•RNA.

Collisional cross section calculation. The experimental collisional cross sections (CCSs) were measured in a travelling wave ion mobility (TWIM) drift cell filled with N_2 gas. C-reactive protein, transthyretin, β-lactoglobulin A, alcohol dehydrogenase, concanavalin A and avidin were purchased from MilliporeSigma and used as calibrants. HfqΔCTD, Hfq and calibrants were buffer exchanged and charge reduced by triethylamine acetate as described previously. Theoretical CCSs of calibrants were obtained from a database of charge-reduced proteins (6). The calculated CCSs of analytes were simulated using projected superposition approximation (PSA) on the webserver: http://psa.chem.fsu.edu/ (7). The PDB structure 1hk9 was used as a model for HfqΔCTD (8). Model 1 from the MD simulations in this work (Fig. S4) and previously published Rosetta structures (9) were used as models for Hfq.

MD simulations. All simulations were performed with the molecular dynamics program OpenMM (10). The top 10 models of full-length *E. coli* Hfq previously obtained with Rosetta FloppyTail (9) were used as starting structures for the MD simulations (models 1-10). CHARMM-GUI (11) was used for system setup – the structures were embedded in a water box with an additional 15 Å layer of water in each direction, and charge neutralized with 150 mM NaCl. An additional 4 simulations (extended models e1-e4) were performed by starting from an extended model of the CTDs. The initial extended model was created by prepending or appending N and C-terminal residues in a beta conformation (9) to the core of *E. coli* Hfq (1HK9; (8)). A 10 Å layer of water was added in each direction, and 150 mM NaCl. The protein structures quickly collapsed, so the effective water layer in the simulations was larger. While two of the extended simulations were stopped after 110 ns, two simulations starting from the extended state were simulated further. The structures obtained after 177 ns (for e1) and 100 ns (for e4) were embedded in a smaller water box after the structures collapsed, with a 15 Å layer of water in each direction. This increased the speed of the simulations. The simulations were performed in an NpT ensemble, using the particle mesh Ewald method for electrostatic interactions with a real space interaction cutoff of 12 Å. We used CHARMM36m, an improved force-field for folded and intrinsically disordered proteins (12), with the TIP3P water model. The radius of gyration rapidly decreased to ~30 Å during the first 100 ns (Fig. S3). After this point, the radius of gyration changed little over the remaining simulation time. The first 100 ns were not included in the analysis of the simulation results. Models 1, 3 and 5 were run for additional 1400 ns, models 2 and 4 were run for an additional 400 ns, models 6-10 were run for an additional 100 ns. Two extended models were run for an additional 10 ns, while two extended models that were re-solvated were run for an additional 1000 ns. The simulation lengths are summarized in Table S2.

MD analysis. To gain information about the structures and their evolution, we analyzed contacts between the CTDs and the cores of the Hfq subunits during various intervals of the simulation (Figs. S7-S8). A CTD of a subunit was considered to contact the core (res 1-65) or CTD (res 66-102) of another subunit if, during the time interval of consideration, the distance between any atom of that CTD and any atom of the core (or another CTD) was less than 4 Å. Root mean square deviations (RMSD) from the collapsed CTD structure were calculated at timesteps of 1 ns. For models 1-5, the structure at 100 ns was used as the reference structure. For e1 and e2, the structure 100 ns after restart in the smaller water box was used as the reference. RMSD values were calculated for heavy atoms in individual CTD residues as listed in the figure (Fig. S5- S6).

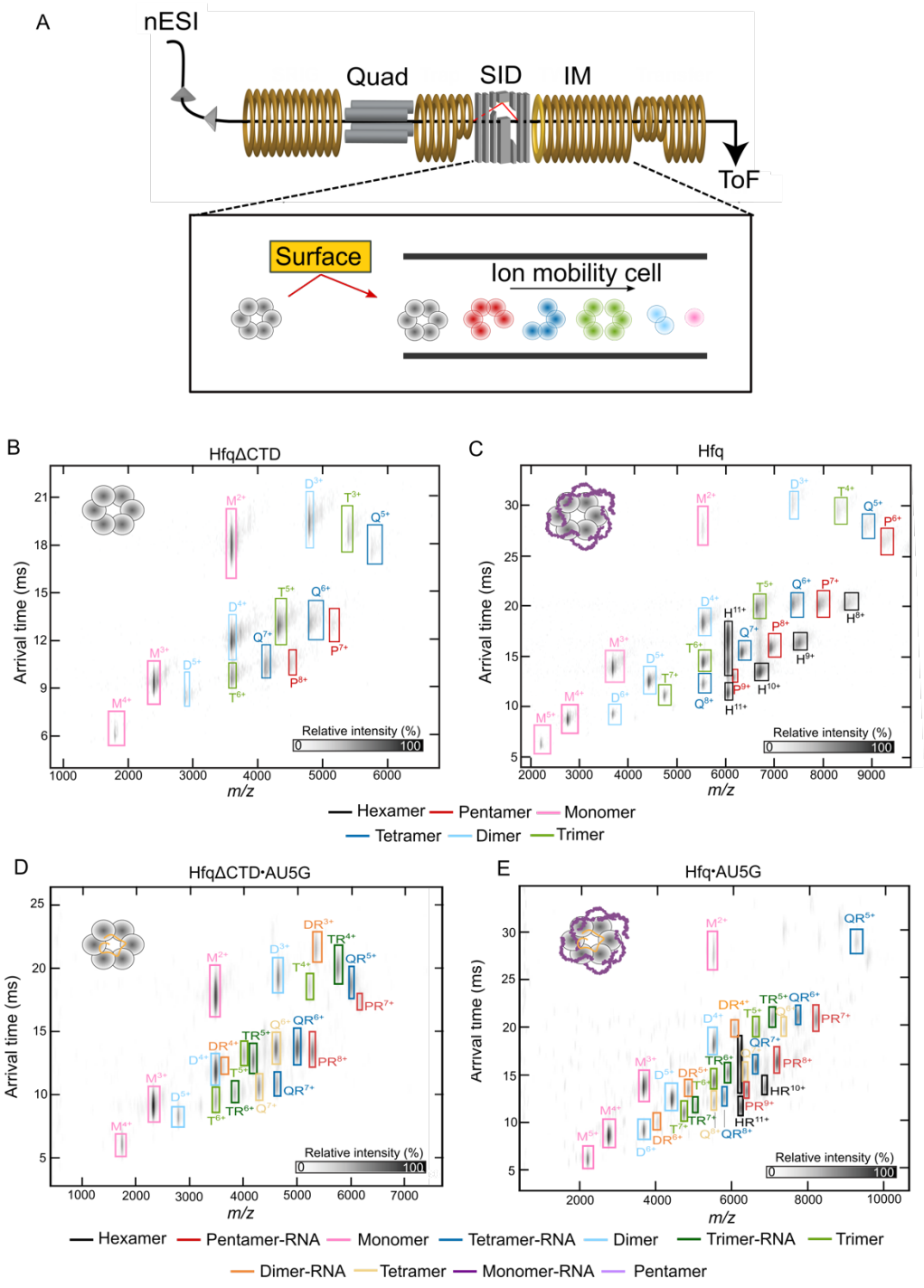

Fig. S1. Separation of dissociated complexes by ion mobility. (*A*) Schematic of native mass spectrometer with surface-induced dissociation (nMS-SID) (1). Intact complexes undergo nano electrospray ionization (nESI) followed by selection of a precursor charge state with a quadrupole mass filter (Quad). The selected complex collides with a gold surface with a self-assembled monolayer (SID; red path). The resulting fragment ions along with the remaining precursor ions are separated based on mass, shape and charge in an ion mobility cell (IM) and analyzed in a time-of-flight analyzer (ToF) with results reported in an ion mobiligram. The black path through

the SID module indicates the trajectory of the complexes when the instrument is in transmission mode (no collisions). (*B*-*E*) Ion mobiligrams of (*B*) HfqΔCTD at SID 605 eV, (*C*) Hfq at SID 608 eV, (*D*) HfqΔCTD•AU_5G RNA at SID 613 eV, and (*E*) Hfq •AU_5G RNA at SID 624 eV. The mobiligrams report the time needed to traverse an ion mobility cell and reach the detector (arrival time) versus the mass-to-charge ratio of the various fragments. Certain complexes overlap in mass-to-charge but are characterized by unique arrival times, signaling different oligomeric states: pentamer (P), tetramer (Q), trimer (T), dimer (D), and monomer (M). Cases in which a given fragment (for example, hexamer, H) has the same *m/z* but different arrival times represent different conformations, with the slower drift characteristic of more extended conformations.

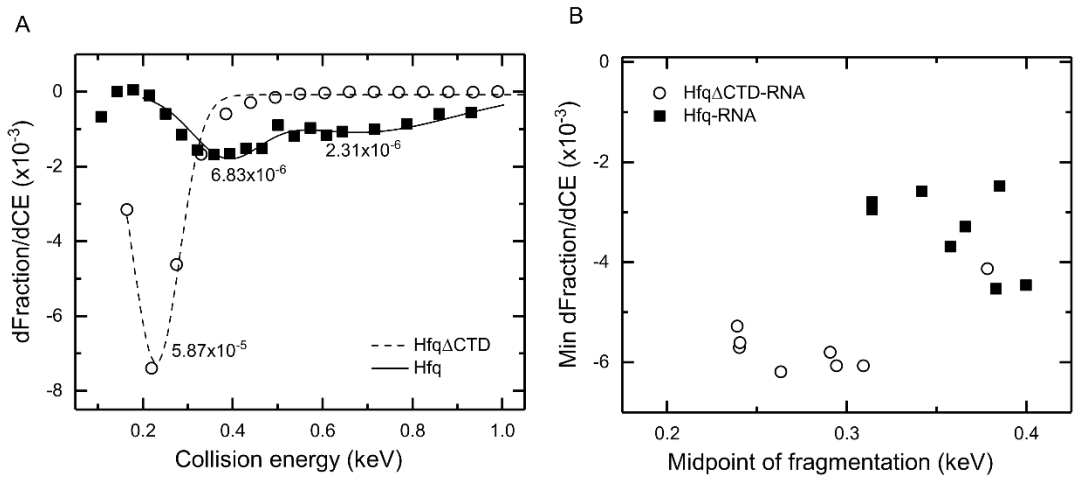

Fig. S2. Steepness of protein fragmentation by SID. (*A*) Derivative of the hexamer fraction with respect to collision energy for HfqΔCTD (open round symbols, dashed line) and Hfq (closed square symbols, solid line) (see also Figs. 2*B*-*C*). The lines are Gaussian fits used to calculate the ratio of the minimum of the derivative over the FWHM of the curve for each of the transitions observed (numbers reported in the curve). Fragmentation of Hfq is best represented by two Gaussian functions. (*B*) Fragmentation of RNA complexes. Minimum value of the derivative of the hexamer fraction (reporting the steepness of the fragmentation) vs the collision energies at which those minimum values occur (midpoint of fragmentation) for HfqΔCTD (open round symbols) and Hfq (closed square symbols) bound to various RNAs (see also Figs. 4*A, B* and *D*). Each data point corresponds to the respective protein bound to a different RNA. For Hfq•RNA complexes, steepness correlates poorly with the midpoint of the fragmentation curve.

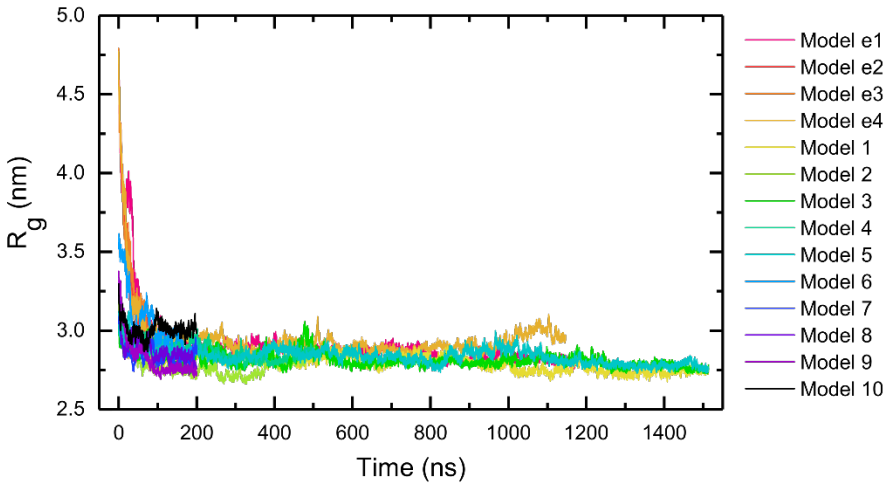

Fig. S3. Hfq compaction from MD simulations. Time evolution of the radius of gyration (R_g) of Hfq, for different starting models. Extended models e1, e4 were run for slightly over 1100 ns, e2, e3 were run for 110 ns, Rosetta models 1, 3, 5 for 1500 ns, 2, 4 for 500 ns and models 6-10 for 200 ns (Table S2). All models collapsed to more compact structures (R_g ~ 27-31 Å) in the first 100 ns, except for e4, which was after 177 ns. The structures remained compact for the remainder of the simulation time although the actual positions of the CTDs changed. Because the CTDs are intrinsically disordered and mobile, the models do not converge to any single structure.

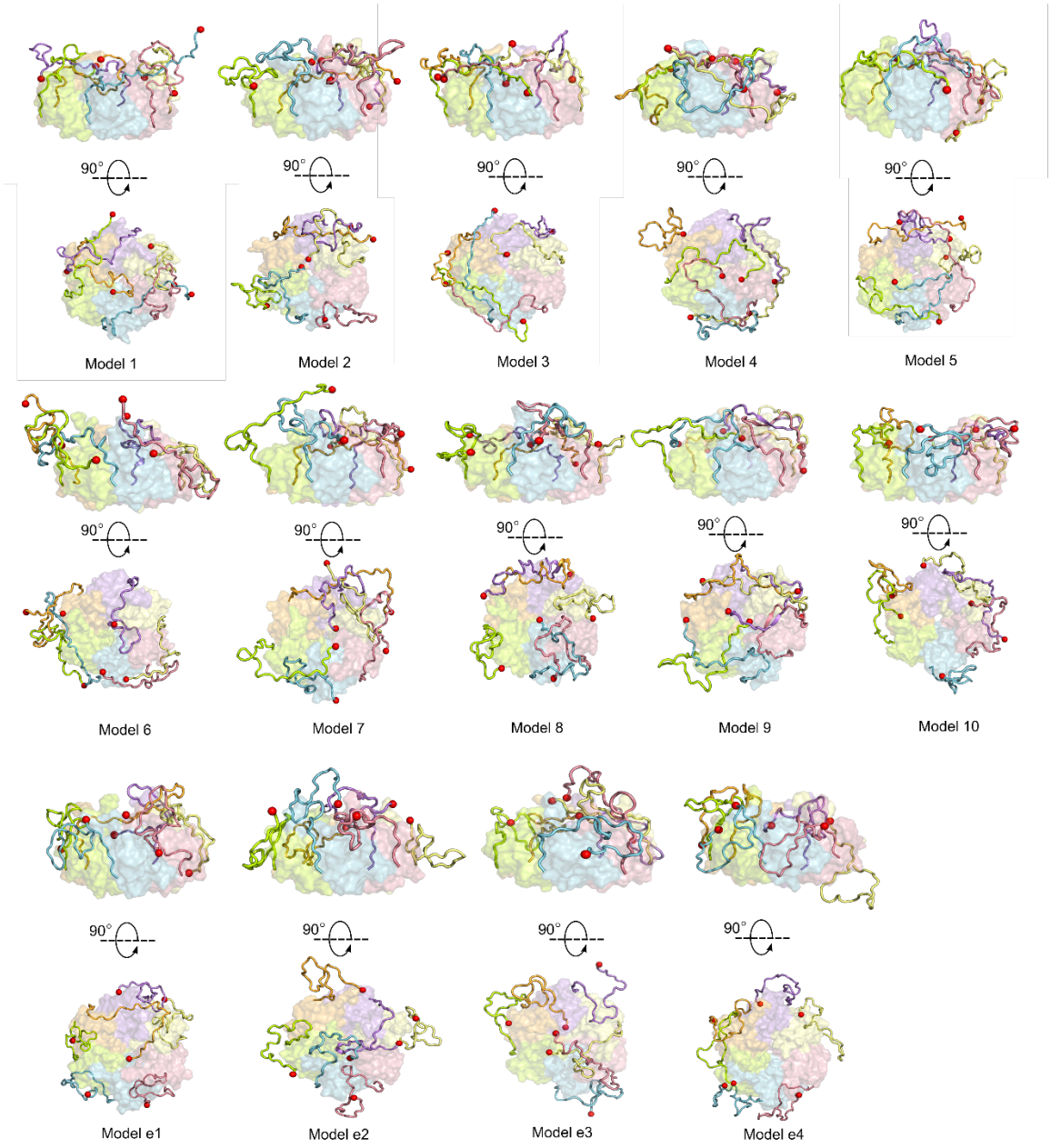

Fig. S4. Structures of *E. coli* Hfq from MD simulations. Top and side views of Hfq models from 14 MD runs. Subunits and their CTDs are colored individually with each acidic tip shown as a red sphere. The structures shown are from the last frame of each simulation: 1500 ns for models 1,3,5; 500 ns for models 2,4; 200 ns for models top 6-10; 1000 ns for models e1, e4, and 110 ns for models e2-e3.

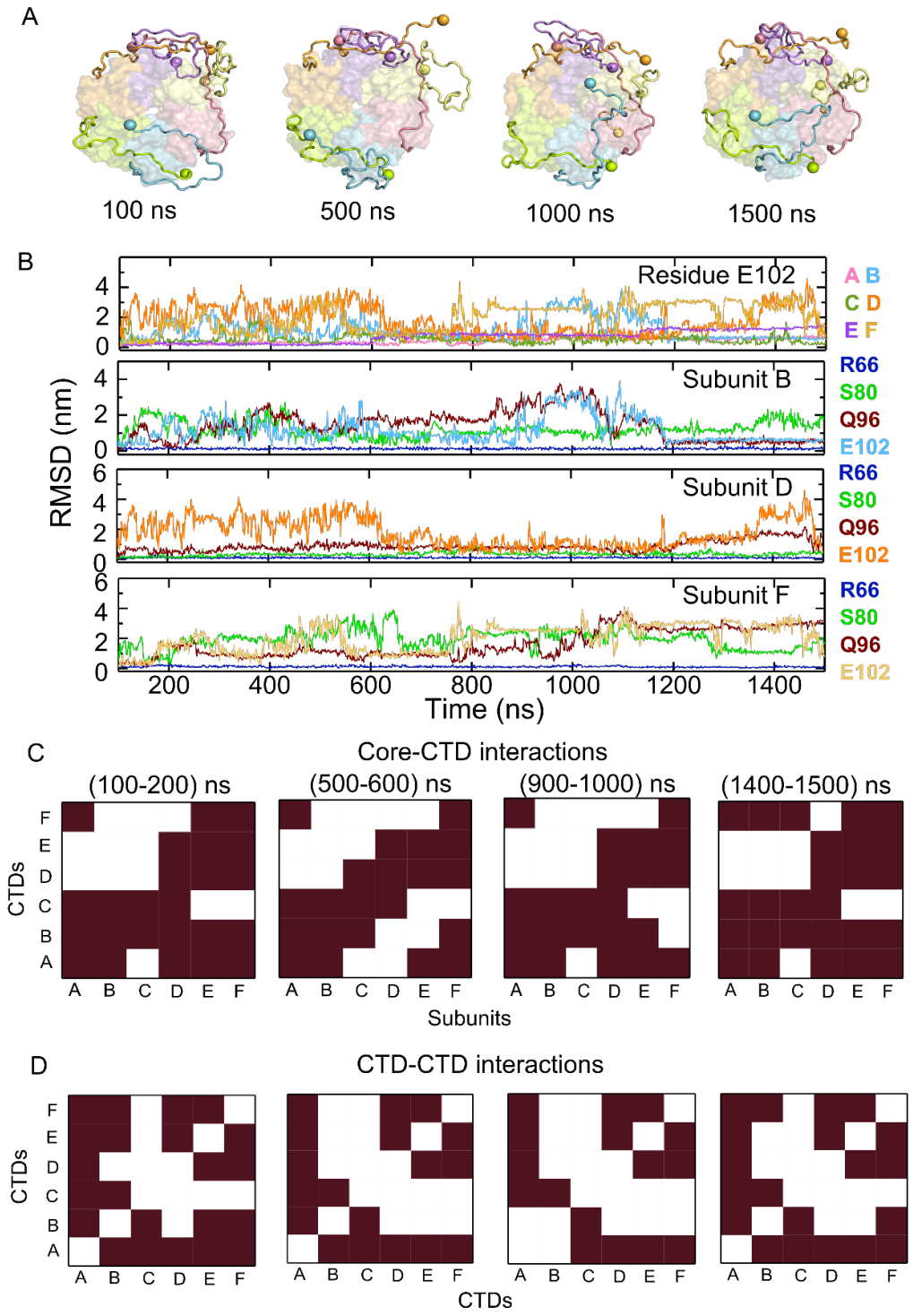

Fig. S5. Time evolution of CTD interactions from MD simulations. Results are shown for model 5 (1.5 μs total). Comparable results were obtained for other models. The first 100 ns prior to collapse of *R*g is not shown. (*A*) Snapshots of Hfq at 100, 500, 1000 and 1500 ns. The C-terminus of each chain is rendered as a colored sphere. (*B*) Root mean square deviation (RMSD) relative to the structure at 100 ns over time for individual CTD residues (see SI Methods). Top panel, RMSD for C-terminal E102 for each subunit. Colors for chains A-F as in (*A*). Lower panels

compare the position of R66, S80, Q96 and E102 for chains B, F and D. As expected, R66 adjacent to the folded core domains is the least mobile, whereas Q96 and E102 at the tip show the greatest variation. (*C-D)* Matrices comparing the subunit interactions of each CTD, at 100, 500, 1000 and 1500 ns of the simulation. (*C*) CTDs interacting with core domains of each subunit. A colored block indicates that at least one residue in the CTD interacts with one residue of the core in any frame, as also shown in Fig. S7. (*D*) CTD-CTD interactions, as in *C*. The different patterns in the grid indicate a change in inter-subunit interactions during the simulation.

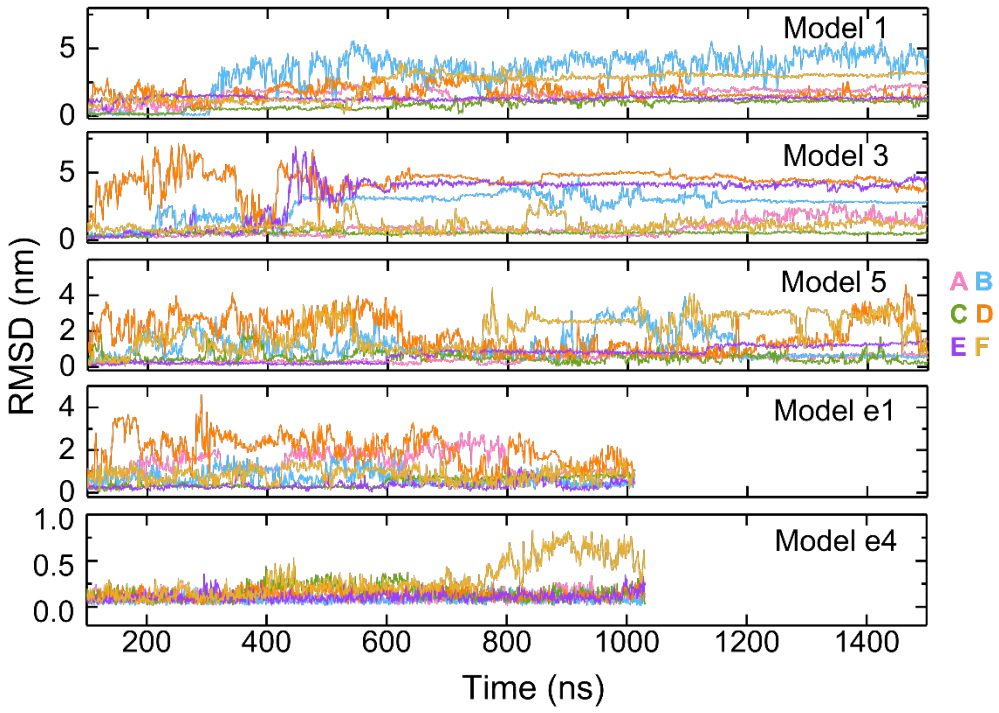

Fig. S6. Time evolution of CTD interactions from MD simulations in different models. Root mean square deviation (RMSD) of residue E102 over time for models 1, 3, 5, e1 and e4, as in Fig. S5B. Colors correspond to the subunits as in Fig. S5A. Individual CTDs transition between periods of low and high mobility, but the moment of these transitions differs in each model.

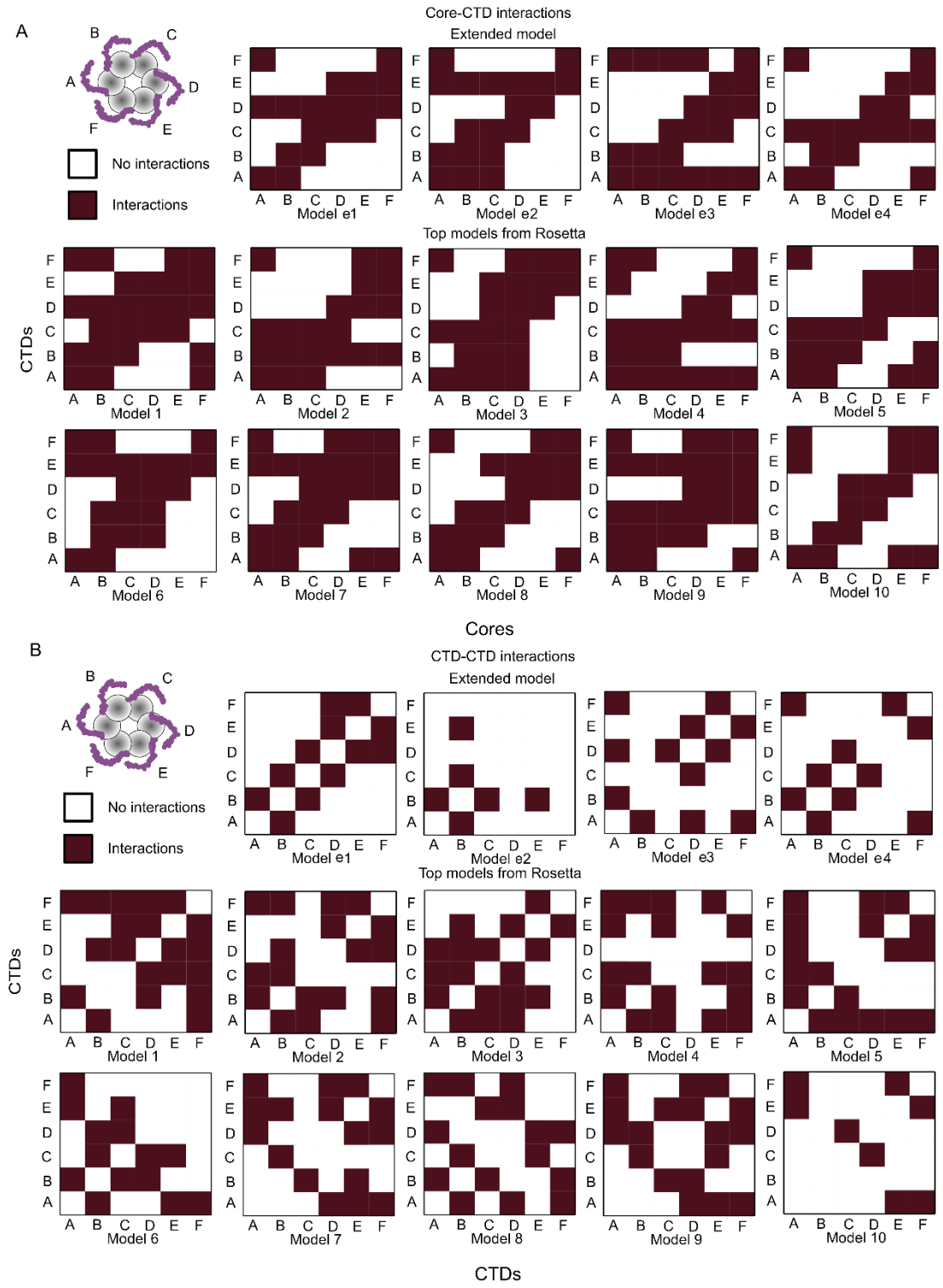

Fig. S7. Interactions between CTDs and Hfq cores from MD simulations. (*A)* Core interactions of each CTD are shown, for the 14 starting models. Colored squares indicate that at least one residue in the CTD (66-102 aa) interacts with one core residue (1-65 aa) of a given chain in any frame of the first 100-110 ns of the simulation, for each model. (*B)* Interactions between CTDs. Colors indicate that at least one residue in a CTD interacts with one residue of another CTD in any frame of the first 100-110 ns. The 6 subunits are labeled A-F, as illustrated in the cartoon.

The varied patterns show the diversity of inter-chain interaction patterns among the models. For examples of the interactions at other intervals of the simulation see Fig. S5C. The CTDs are less entangled when starting from extended models than from Rosetta models, but these models still form a substantial number of inter-subunit interactions as the simulation continues (Fig. S8).

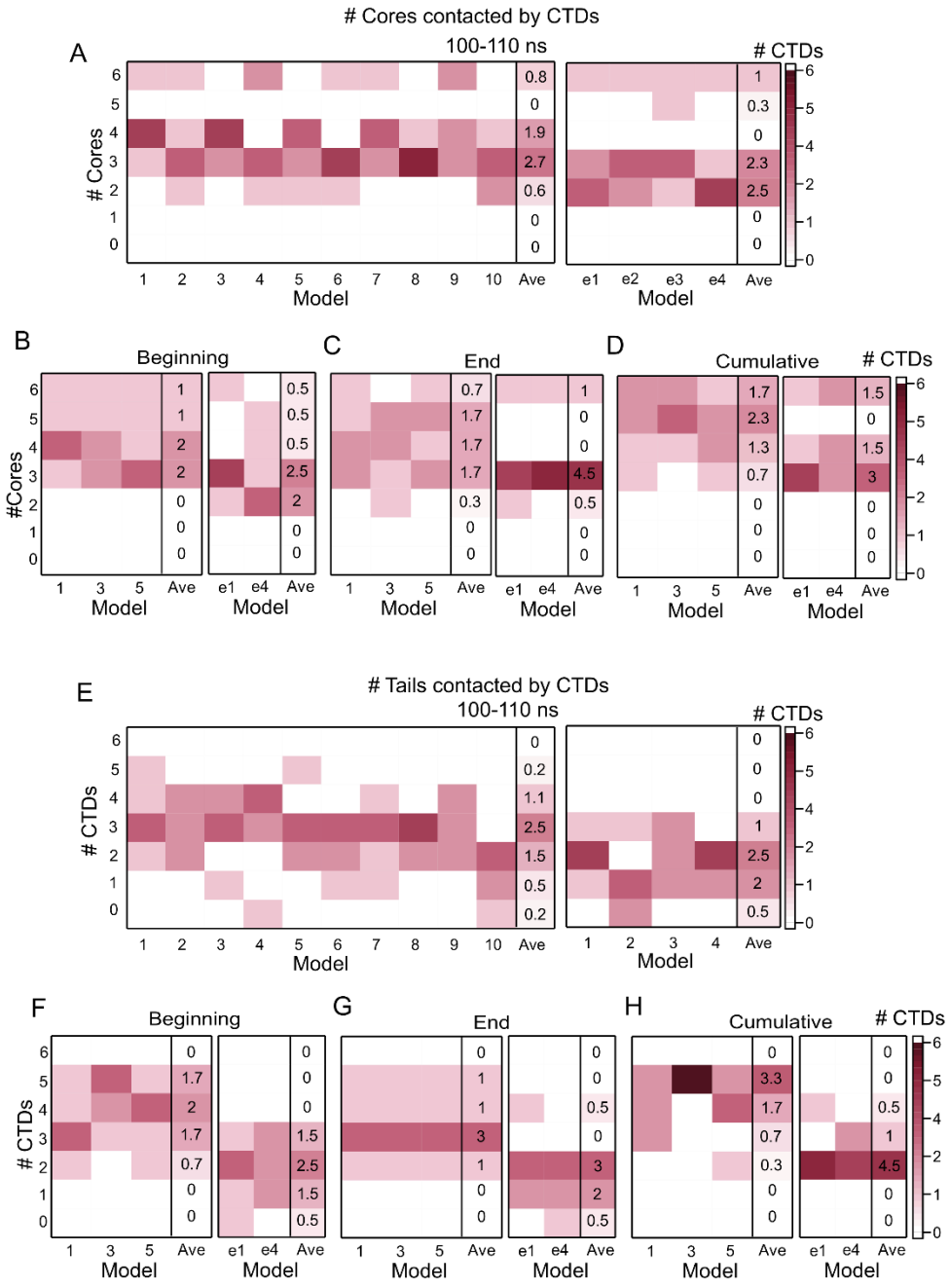

Fig. S8. Summary of interchain interactions from MD simulations. Disordered CTDs establish multiple interactions across Hfq. The heat map colors indicate the number of CTDs within each hexamer that interact with 1, 2, 3, 4, 5, or 6 (*A-D*) core domains or (*E-H*) CTDs, for the models indicated beneath the plots. For example, in model 1 at the left of panel A, one CTD contacts 3 core domains, 4 CTDs contact 4 core domains and 1 CTD contacts 6 core domains. (*A, E*) the first 10 ns after equilibration for all MD models, (*B, F*) the first 100 ns after equilibration, (*C-G*) the last 100 ns, and (*D-H*) the whole simulation, for the longest simulations. The average of the number of interactions (Ave) starting from Rosetta structures or extended models is shown at the right of each heat map.

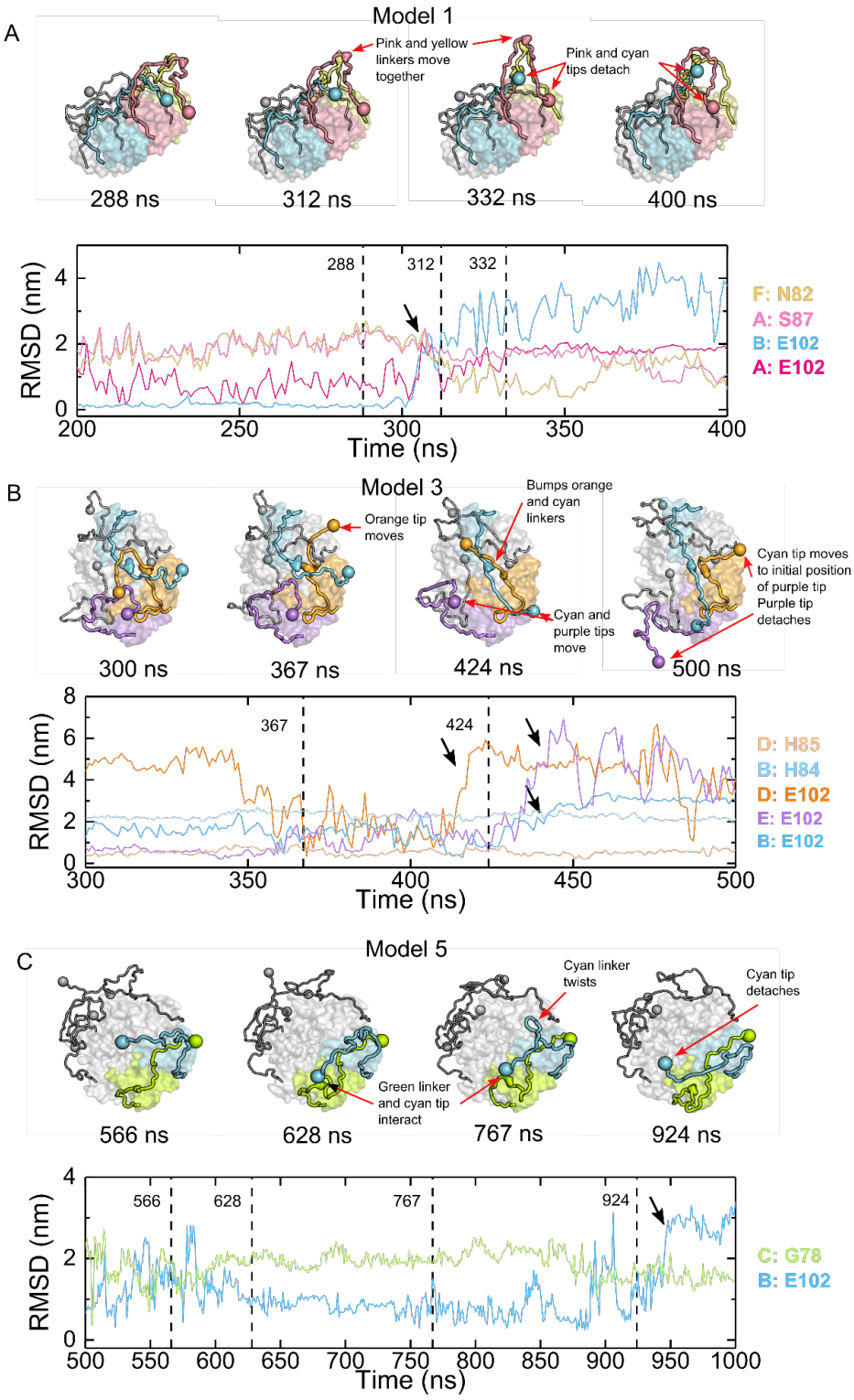

Fig. S9. Representative examples of CTD interconnections. (*A*-*C*) Snapshots of structures at various times of the MD simulations, and RMSD values of residues involved in CTD-CTD interactions that correlate with changes in the contacts made by other CTDs. See also Supplemental Movies 1-4. (*A*) In model 1, the linker regions of the CTDs from the pink and yellow subunits move together (representative residues, N82 and S87, from 200-400 ns), seemingly

causing the tips (E102) of the pink and cyan CTDs to detach (312-400 ns). (*B*) In model 3, the tip of the orange CTD moves around (300-500 ns) while its linker (H85) interacts with the linker of the cyan CTD (H84, from 300-500 ns), also affecting the cyan tip (424-500 ns), which moves toward the purple tip. The purple tip is displaced (424-500 ns). (*C*) In model 5, the linker of the green CTD (G78) and the tip of the cyan CTD establish an interaction (628-767 ns), that results in the twisting of the linker of the cyan CTD(767 ns). The strain caused by this twist likely triggers the detachment of the cyan tip (924 ns). Colors in the RMSD curves correspond to the color of each subunit in the ribbons (A: pink, B: cyan, C: green, D: orange, E: purple, or F: yellow). Tip detachments correspond to large increases in RMSD (arrows). Dashed lines in the RMSD plots match the times of the snapshots presented.

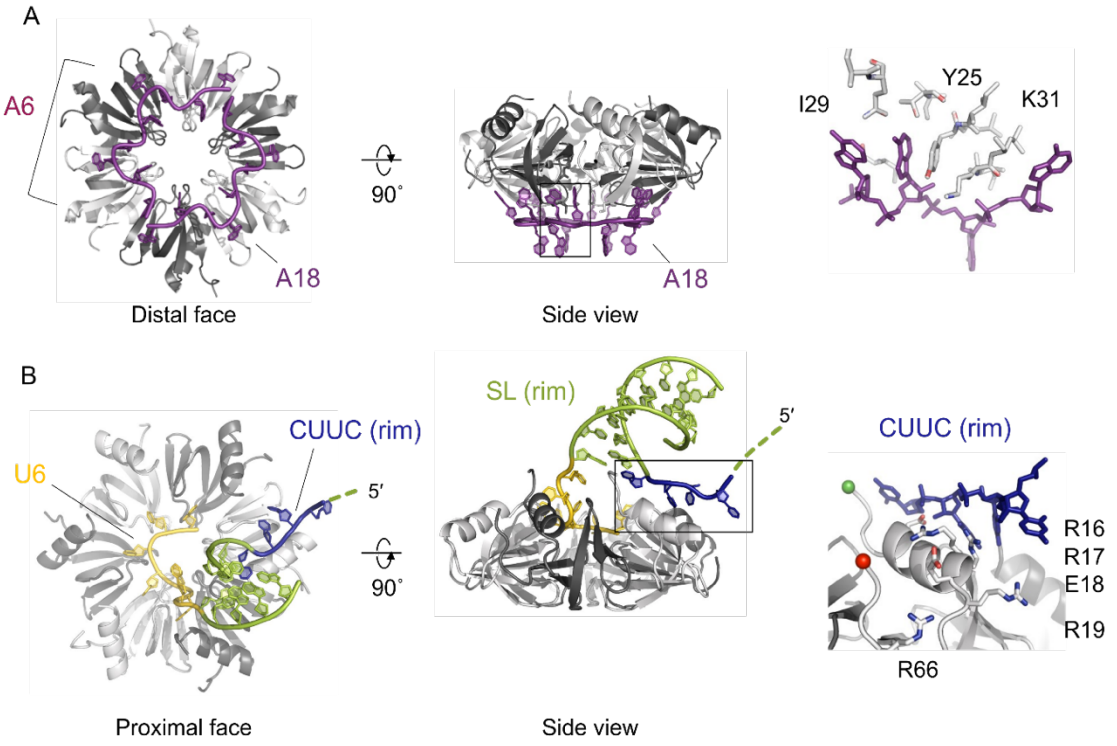

Fig. S10. RNA interactions with Hfq. Each surface of Hfq binds a different RNA sequence motif. Natural sRNA and mRNA substrates can interact with more than one surface of Hfq at the same time, forming kinetically stable complexes. (*A*) rA_{18} bound to the distal face with three nucleotides per Hfq subunit, from 3GIB (13). rA_6 is expected to only bind two subunits. (*B*) RydC sRNA bound to the proximal face and rim, from 4V2S (14). The 3′ terminal uridines (gold) bind around the proximal pore (1 base per subunit). The terminal stem-loop (SL; green) sits atop the proximal face, and the single-stranded CUUC motif (blue) interacts with the arginine patch on the rim of the hexamer. RybB sRNA and the minimal rim-SL RNA used in this study contain similar sequences and are expected to bind Hfq similarly. The RNAs are color-coded as in Fig. 4*A*.

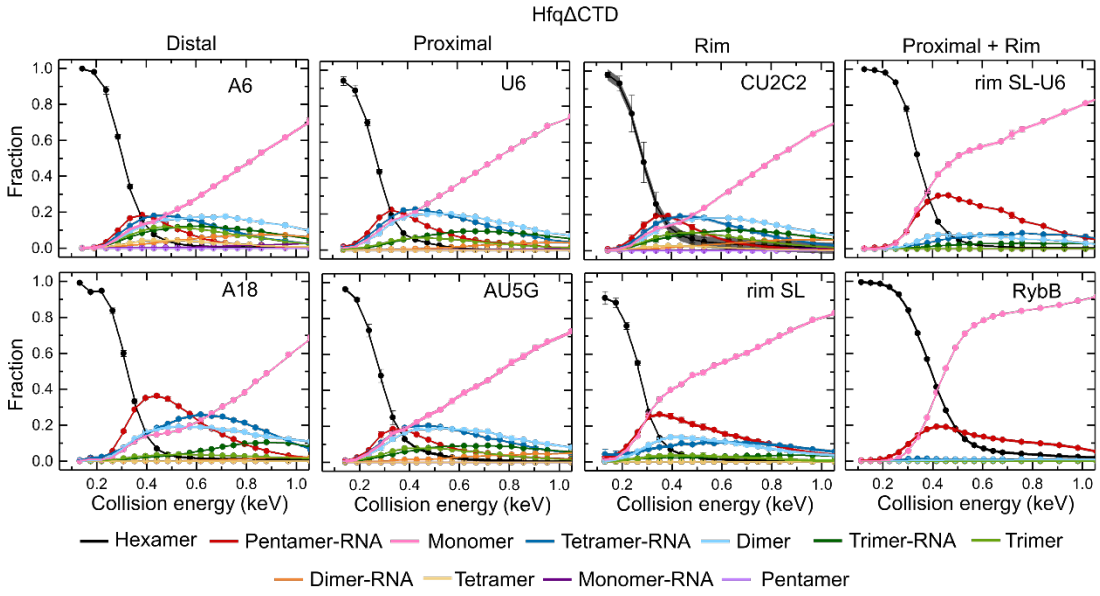

Fig. S11. RNA binding stabilizes Hfq's core. Energy-resolved mass spectra (ERMS) of HfqΔCTD bound to the indicated RNAs. The collision energies are corrected to account for the mass of the RNAs ($\boldsymbol{m_{HfqΔCTD}/m_{HfqΔCTD\cdot RNA}}$). Reported fractions are the sum of the intensities of each dissociation product (from ion mobiligrams; see Fig. S1D for an example) normalized by the total intensity of all products. Symbols report the average of three replicates and the standard errors, which are smaller than symbols for some data points. Solid lines represent a linear interpolation of the data. The spread (negligible) on the interpolated line represents the mean of the errors of individual data points.

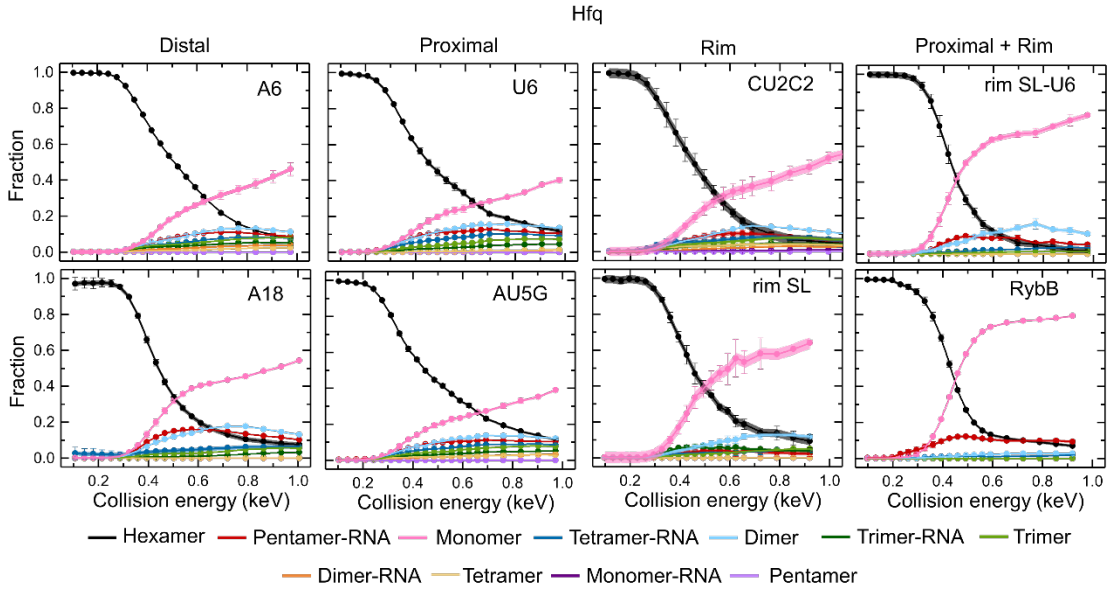

Fig. S12. RNA binding destabilizes Hfq. Energy-resolved mass spectra (ERMS) of Hfq bound to the indicated RNAs. The collision energies are corrected to account for the mass of the RNAs ($\boldsymbol{m_{Hfq}/m_{Hfq\cdot RNA}}$) and the CTDs ($\boldsymbol{m_{Hfq\Delta CTD}/m_{Hfq}}$). Reported fractions are the sum of the intensities of each dissociation product (from ion mobiligrams; see Fig. S1E for an example) normalized by the total intensity of all products. Symbols report the average of three replicates. Errors are the standard error and are smaller than symbols for some data points. Solid lines represent a linear interpolation of the data. The spread (negligible) on the interpolated line represents the mean of the errors of individual data points.

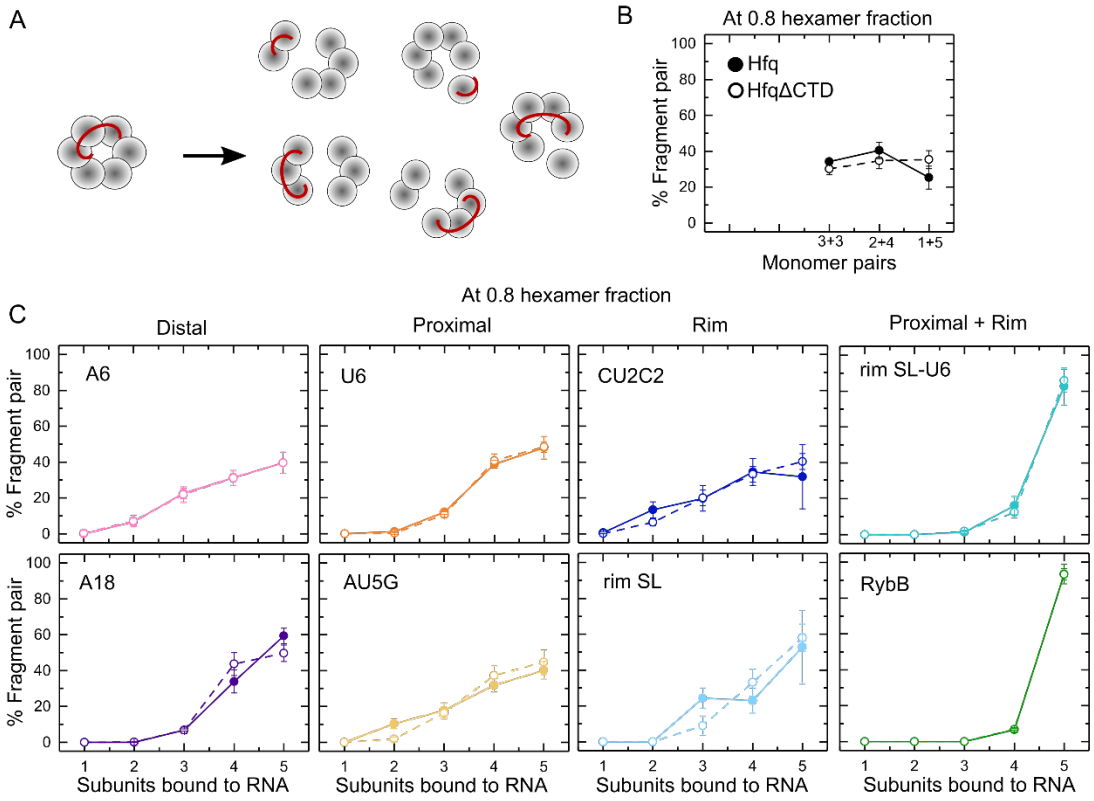

Fig. S13. Dissociation pathways of Hfq complexes. (*A*) Hfq bound to RNA dissociates into different pathways with different fragment pairs (pentamer•RNA + monomer, etc.). (*B*) Percentage of fragment pairs obtained after the collision of Hfq (solid lines) or HfqΔCTD (dashed lines). To minimize contributions from secondary dissociation events, we compared the dissociation products when 20% of the protein was fragmented (0.8 hexamer fraction). (*C*) Percentage of fragment pairs obtained after the collision of Hfq (solid lines) or HfqΔCTD (dashed lines) bound to the indicated RNAs, when 20% of the precursor ion is fragmented. Errors are the addition of the spread of the ERMS curves for the fragment pairs (Figs. S11-S12), normalized by the total dissociated fraction and converted to percentage. Solid lines are a visual guide. %Fragment pair is similar for RNAs bound to both proteins, except for rim SL, in agreement with a decreased CTD perturbation (Fig. 4G, light blue), and for the proximal binding AU_5G, suggesting that the CTDs may detect the RNA as a suboptimal binder (in comparison to U_6).

Table S1. Experimental (TWIM) and calculated (PSA) collision cross sections (CCS) of HfqΔCTD and Hfq.

Protein	TWIM[a]		PSA[a]	
	Charge state	CCS (Å^2)[b]	Model[c]	CCS (Å^2)
HfqΔCTD	10+	3341±17	PDB:1hk9	3243
	9+	3278±12		
Hfq	12+	4125±19	MD	4473±129[d]
	11+	4096±14	Rosetta	5539

[a]TWIM: Traveling wave ion mobility. PSA: Projected superposition approximation.

[b]Error of TWIM is shown as standard deviation of triplicate measurements.

[c]Models for calculated CCS: PDB from database (https://www.rcsb.org/) and Sauter et al. (8); MD from this work (models 1-5 at 500 ns); Rosetta from Santiago-Frangos et al. (9).

[d]PSA-calculated CCS of Hfq is shown as average and standard deviation of models 1-5 from MD simulations.

Table S2. Molecular dynamics simulation parameters.

Model	Starting model[a]	Length of simulation (ns)
1	Rosetta top 1	1,500
2	Rosetta top 2	500
3	Rosetta top 3	1,500
4	Rosetta top 4	500
5	Rosetta top 5	1,500
6	Rosetta top 6	200
7	Rosetta top 7	200
8	Rosetta top 8	200
9	Rosetta top 9	200
10	Rosetta top 10	200
e1	Hfq with extended CTDs 1	1,013
e2	Hfq with extended CTDs 2	110
e3	Hfq with extended CTDs 3	110
e4	Hfq with extended CTDs 4	1,032
Total		8,920

[a]Starting Rosetta models correspond to structures with the lowest free energies as produced in (9).

Table S3. Sequences of RNAs used in this work.

RNA	Sequence (5'→3')
rA_6	AAAAAA
rA_{18}	AAAAAAAAAAAAAAAAAA
rU_6	UUUUUU
rAU_5G	AUUUUUG
rCU_2C_2	CUUCC
rim SL	CUUCCGUCCAUUUCGGACG
rim SL-U_6	CUUCCGUCCAUUUCGGACGUUUUUU
RybB[a]	gGCCACUGCUUUUCUUUGAUGUCCCCAUUUUGUGGAGCCCAUCAACCCCGCCAUUU CGGUUCAAGGUUGAUGGGUUUUUU

[a]Nucleotides in lowercase letters were added to the natural RybB sequence to facilitate *in vitro* transcription by T7 polymerase.

Table S4. Typical voltage parameters on components of the modified Waters SYNAPT G2 mass spectrometer used in this work for surface-induced dissociation (SID).

Component	Voltage (V)		
	Transmission mode[a]	SID 15 (V)	SID 15+x* (V)[b]
Trap bias	45	75	75+x*
Trap exit	-40	-15	-15+x*
Entrance 1	-42	-15	-15+x*
Entrance 2	-44	-46	-46
Front top	-63	-56	-56
Front bottom	-64	-15	-15+x*
Middle bottom	-61	-46	-46
Surface	-59	-30	-30
Rear top	-60	-170	-170
Rear bottom	-61	-55	-55
Exit 1	-73	-67	-67
Exit 2	-74	-77	-77

[a]Transmission mode: The complexes are not made to collide with the soft surface, instead directly passing to the ion mobility cell (Fig. S1*A*).

[b]x*: SID voltage increment compared to SID 15V. To produce higher SID voltages, the voltages applied on the trap cell and two SID lens were increased.

Table S5. Parameters used for nMS-SID experiments.

Parameter	Value
Sampling cone voltage	20 V
Extraction cone voltage	2 V
Source temperature	30 °C
Trap gas flow	2 mL/min
Ion mobility gas flow	60 mL/min
Ion mobility wave velocity	320 m/s
Ion mobility wave height	20 V

Supplementary Movie 1

MD trajectory for model 1 from 100 – 1500 ns, rendered as in Fig. S4. Water and ions are not shown.

Supplementary Movie 2

MD Trajectory for model 3 from 100 – 1500 ns.

Supplementary Movie 3

MD Trajectory for model 5 from 100 – 1500 ns.

Supplementary Movie 4

MD Trajectory for model 3 from 100 – 1500 ns, with CTDs rendered as a van der Waals surface.

Dataset S1 (separate file). Data underlying the plots in the main figures and supplemental figures, as a tab-delimited spreadsheet.

Fig. 2B: Energy-resolved mass spectrum (ERMS) of HfqΔCTD.
Fig. 2C: Energy-resolved mass spectrum (ERMS) of Hfq.
Fig. 2D: Percentage of HfqΔCTD fragments as a function of the hexamer fraction.
Fig. 2E: Percentage of Hfq fragments as a function of the hexamer fraction.
Fig. 2F: Surface induced unfolding (SIU) of HfqΔCTD.
Fig. 2G: Surface induced unfolding (SIU) of Hfq.
Fig. 3B: Average number of CTDs contacting various Hfq subunits during MD simulations.
Fig. 3C: Average number of CTDs contacting other Hfq CTDs during MD simulations.
Fig. 4B: Energy-resolved mass spectra (ERMS) of HfqΔCTD bound to various RNAs.
Fig. 4C: Collision energy difference (ΔCE) between free and RNA-bound HfqΔCTD at various fractions of the hexamer.
Fig. 4D: Energy-resolved mass spectra (ERMS) of Hfq bound to various RNAs.
Fig. 4E: Collision energy difference (ΔCE) between free and RNA-bound Hfq at various fractions of the hexamer.
Fig. 4F: Energy-resolved mass spectra (ERMS) of HfqΔCTD and Hfq free and bound to RybB.
Fig. 5C: Stabilities of Hfq, HfqΔCTD and CTD when bound to RNAs mimicking progressive RNA binding.
Fig. S1B: Representative ion mobiligram of HfqΔCTD at 605 eV.
Note: Intensities versus arrival time or m/z of the subcomplexes were obtained with TWIMExtract v1.3, as explained in Methods. Mobiligrams were plotted directly using ORIGAMI 1.2.1.6.

Fig. S1C: Representative ion mobiligram of Hfq at 608 eV.
Note: Intensities versus arrival time or m/z of the subcomplexes were obtained with TWIMExtract v1.3, as explained in Methods. Mobiligrams were plotted directly using ORIGAMI 1.2.1.6.
Fig. S2A: Derivative of the hexamer fraction with respect to collision energy for HfqΔCTD and Hfq.
Fig. S2B: Minimum value of the derivative of the hexamer fraction vs midpoint of fragmentation for HfqΔCTD and Hfq bound to various RNAs.
Fig. S3: Evolution of radius of gyration (Rg) of Hfq from MD simulations.
Fig. S5B: RMSD of various CTDs residues from a single model from MD simulations.
Fig. S5C: Individual interactions between CTDs and subunits of Hfq from a single model for various time points from MD simulations.
Fig. S5D: Individual interactions between CTDs of Hfq from a single model for various time points from MD simulations.
Fig. S6: RMSD of a single CTD residue for various models from MD simulations.
Fig. S7A: Individual interactions between CTDs and cores of Hfq from MD simulations.
Fig. S7B: Individual interactions between CTDs of Hfq from MD simulations.
Fig. S8A-D: Number of CTDs interacting with various cores of Hfq from MD simulations
Fig. S8E-H: Number of CTDs interacting with other CTDs of Hfq from MD simulations.
Fig. S9A: RMSD plots for representative residues involved in connected CTD-CTD interactions for model 1.
Fig. S9B: RMSD plots for representative residues involved in connected CTD-CTD interactions for model 3.
Fig. S9C: RMSD plots for representative residues involved in connected CTD-CTD interactions for model 5.
Data for Fig. S11 was included in a single spreadsheet for individual plots, labeled a-h:
Fig. S11a: Energy-resolved mass spectrum (ERMS) of HfqΔCTD bound to A6.
Fig. S11b: Energy-resolved mass spectrum (ERMS) of HfqΔCTD bound to A18.
Fig. S11c: Energy-resolved mass spectrum (ERMS) of HfqΔCTD bound to U6.
Fig. S11d: Energy-resolved mass spectrum (ERMS) of HfqΔCTD bound to AU5G.
Fig. S11e: Energy-resolved mass spectrum (ERMS) of HfqΔCTD bound to CU2C2.
Fig. S11f: Energy-resolved mass spectrum (ERMS) of HfqΔCTD bound to rim SL.
Fig. S11g: Energy-resolved mass spectrum (ERMS) of HfqΔCTD bound to rim SL-U6.
Fig. S11h: Energy-resolved mass spectrum (ERMS) of HfqΔCTD bound to RybB.
Data for Fig. S12 was included in a single spreadsheet for individual plots, labeled a-h:
Fig. S12a: Energy-resolved mass spectrum (ERMS) of Hfq bound to A6.
Fig. S12b: Energy-resolved mass spectrum (ERMS) of Hfq bound to A18.
Fig. S12c: Energy-resolved mass spectrum (ERMS) of Hfq bound to U6.
Fig. S12d: Energy-resolved mass spectrum (ERMS) of Hfq bound to AU5G.
Fig. S12e: Energy-resolved mass spectrum (ERMS) of Hfq bound to CU2C2.
Fig. S12f: Energy-resolved mass spectrum (ERMS) of Hfq bound to rim SL.
Fig. S12g: Energy-resolved mass spectrum (ERMS) of Hfq bound to rim SL-U6.
Fig. S12h: Energy-resolved mass spectrum (ERMS) of Hfq bound to RybB.
Fig. S13B: Percentage of fragment pairs from HfqΔCTD and Hfq dissociation.
Fig. S13C: Percentage of fragment pairs from HfqΔCTD-RNA and Hfq-RNA dissociation.

Dataset S2 (separate file). Raw ion mobiligrams, related to Fig. S1B.

SI References

1. M. Zhou, C. Huang, V. H. Wysocki, Surface-induced dissociation of ion mobility-separated noncovalent complexes in a quadrupole/time-of-flight mass spectrometer. *Anal. Chem.* **84**, 6016–6023 (2012).
2. M. T. Marty, *et al.*, Bayesian deconvolution of mass and ion mobility spectra: From binary interactions to polydisperse ensembles. *Anal. Chem.* **87**, 4370–4376 (2015).
3. S. E. Haynes, *et al.*, Variable-Velocity Traveling-Wave Ion Mobility Separation Enhancing Peak Capacity for Data-Independent Acquisition Proteomics. *Anal. Chem.* **89**, 5669–5672 (2017).
4. A. R. Dongré, J. L. Jones, Á. Somogyi, V. H. Wysocki, Influence of peptide composition, gas-phase basicity, and chemical modification on fragmentation efficiency: Evidence for the mobile proton model. *J. Am. Chem. Soc.* **118**, 8365–8374 (1996).
5. L. G. Migas, A. P. France, B. Bellina, P. E. Barran, ORIGAMI: A software suite for activated ion mobility mass spectrometry (aIM-MS) applied to multimeric protein assemblies. *Int. J. Mass Spectrom.* **427**, 20–28 (2018).
6. A. Q. Stiving, B. J. Jones, J. Ujma, K. Giles, V. H. Wysocki, Collision Cross Sections of Charge-Reduced Proteins and Protein Complexes: A Database for Collision Cross Section Calibration. *Anal. Chem.* **92**, 4475–4483 (2020).
7. C. Bleiholder, S. Contreras, M. T. Bowers, A novel projection approximation algorithm for the fast and accurate computation of molecular collision cross sections (IV). Application to polypeptides. *Int. J. Mass Spectrom.* **354**–**355**, 275–280 (2013).
8. C. Sauter, J. Basquin, D. Suck, Sm-like proteins in Eubacteria: The crystal structure of the Hfq protein from Escherichia coli. *Nucleic Acids Res.* **31**, 4091–4098 (2003).
9. A. Santiago-Frangos, J. R. Jeliazkov, J. J. Gray, S. A. Woodson, Acidic C-terminal domains autoregulate the RNA chaperone Hfq. *Elife* **6**, 1–25 (2017).
10. P. Eastman, *et al.*, OpenMM 7: Rapid development of high performance algorithms for molecular dynamics. *PLoS Comput. Biol.* **13**, 1–17 (2017).
11. S. Jo, T. Kim, V. G. Iyer, W. Im, CHARMM-GUI: A Web-Based Graphical User Interface for Computational Chemistry Softwares. *J. Comput. Chem.* **32**, 174–182 (2012).
12. J. Huang, *et al.*, CHARMM36m: An improved force field for folded and intrinsically disordered proteins. *Nat. Methods* **14**, 71–73 (2016).
13. T. M. Link, P. Valentin-Hansen, R. G. Brennan, Structure of Escherichia coli Hfq bound to polyriboadenylate RNA. *Proc. Natl. Acad. Sci.* **106**, 19292–19297 (2009).
14. D. Dimastrogiovanni, *et al.*, Recognition of the small regulatory RNA RydC by the bacterial Hfq protein. *Elife* **3**, 1–19 (2014).